Semi-analytical computation of the acoustic field of a segment of a cylindrically concave transducer in lossless and attenuating media

Başak Ülker Karbeyaz[a)]
Analogic Corporation, 8 Centennial Drive, Peabody, Massachusetts 01960

Eric L. Miller[b)]
Department of Electrical Engineering and Computer Science, Northeastern University, Boston, Massachusetts 02115

Robin O. Cleveland[c)]
Department of Aerospace and Mechanical Engineering, Boston University, Boston, Massachusetts 02115

(Received 12 December 2005; revised 16 November 2006; accepted 20 November 2006)

Conventional ultrasound transducers used for medical diagnosis generally consist of linearly aligned rectangular apertures with elements that are focused in one plane. While traditional beamforming is easily accomplished with such transducers, the development of quantitative, physics-based imaging methods, such as tomography, requires an accurate, and computationally efficient, model of the field radiated by the transducer. The field can be expressed in terms of the Helmholtz-Kirchhoff integral; however, its direct numerical evaluation is a computationally intensive task. Here, a fast semi-analytical method based on Stepanishen's spatial impulse response formulation [J. Acoust. Soc. Am. **49**, 1627–1638 (1971)] is developed to compute the acoustic field of a rectangular element of cylindrically concave transducers in a homogeneous medium. The pressure field, for lossless and attenuating media, is expressed as a superposition of Bessel functions, which can be evaluated rapidly. In particular, the coefficients of the Bessel series are frequency independent and need only be evaluated once for a given transducer. A speed up of two orders of magnitude is obtained compared to an optimized direct numerical integration. The numerical results are compared with Field II and the Fresnel approximation.
[DOI: 10.1121/1.2409489]

PACS number(s): 43.80.Vj, 43.20.Fn, 43.20.Rz, 43.20.Bi [TDM] Pages: 1226–1237

I. INTRODUCTION

Diagnostic ultrasound imaging systems typically employ one-dimensional arrays to form two-dimensional B-scan images. In the axis normal to the image plane, the so-called elevation plane, the elements have a fixed focus that is effected either by the use of elements that are curved or by the use of an acoustic lens. In the image, or scan plane, the elements in the array are electronically steered and focused using delay and sum beamforming. In theory, these arrays are capable of being used for ultrasound computed tomography if the unbeamformed data can be recorded for each element on the array. For ultrasound computed tomography to be effective an accurate physical model of the acoustic field produced by each element of the transducer in the tissue is needed. The field can be expressed in terms of an integral, however, practical computation of the integral is not trivial.

One method that is well suited for evaluating the field of an ultrasound imaging system is the spatial impulse response (SIR). The SIR is defined as the pressure wave at a point in space in response to a velocity impulse on the radiating surface of the transducer.[1–3] The SIR may be convolved with the time derivative of the normal particle velocity to obtain the time pressure distribution. For ultrasound imaging systems, where short duration pulses are employed, the convolution can be carried out quickly. Exact expressions of the SIR have been calculated for transducers of the following shapes: flat pistons, flat sectors, flat polygons, and spherically focused bowls (or segments thereof). An exact expression for the SIR for the cylindrical elements used in imaging arrays has not been forthcoming. Wu and Stepinski[4] proposed modeling cylindrically concave elements as a row of narrow strips, which can be considered as planar rectangular transducers whose exact SIRs are available. This technique still results in two integrals, the convolution in time and the summation over the subelements, but has been effectively employed by the Field II program.[5]

One issue with the SIR is that it cannot directly simulate the field in an attenuating medium. Frequency dependent attenuation (and its concomitant dispersion) has a significant impact on ultrasound propagation in the human body. In the SIR approach, attenuation is typically handled by determining the pressure waveform for a lossless medium and then correcting the waveform by applying a filter, the material transfer function[6] (p. 207), to compensate for attenuation. The implicit assumption is that attenuation and diffraction

[a)]Electronic mail: bulker@ece.neu.edu
[b)]Electronic mail: elmiller@ece.neu.edu
[c)]Electronic mail: robinc@bu.edu

are uncoupled. A time domain method that can be applied to attenuating media is the **d**iscrete **r**epresentation **a**rray **m**odeling (DREAM) procedure, which models arbitrary transducer surfaces as a discrete number of point sources[7] and can be used to model power law type attenuating medium as is appropriate for soft tissue. However, DREAM is computationally intensive as it "trades simplicity, clarity, and generality for increased computational time."[7]

In the frequency domain, the field from an arbitrary flat transducer can be evaluated by means of the angular spectrum technique.[8] However, the angular spectrum technique is very computationally intensive and for transducer elements that are not flat it is necessary to migrate the source condition to a plane. An alternative frequency domain approach is to employ the Fresnel approximation[6] (p. 140), which is computationally efficient but restricts the solution to points that are close to the axis and not too close to the transducer.

We seek a rapid method for calculating the spatial response of a cylindrical radiator in lossy media. Our technique was instigated by the work of Theumann *et al.*,[9] who considered the field inside a cylinder transducer and were able to reduce the surface integral to a single integral in the time domain for which numerical methods were employed to obtain the result. The philosophy here is similar except that the problem is cast in the frequency domain and, for a small cylindrical concave element, a mild approximation to the integrand allows an analytical solution for one of the two integrals to be obtained. The remaining integral is expanded as a truncated series of Legendre polynomials, which are integrated exactly term by term. The resulting response is represented as summation of a small number of Bessel functions and compared to an optimized numerical routine.

II. THEORY: SPATIAL IMPULSE RESPONSE

For a homogeneous fluid medium with a constant sound speed and density, the acoustic field at frequency ω and position $\boldsymbol{r}_p$ is calculated with the use of the velocity potential $\Phi(\boldsymbol{r}_p,\omega)$ and imposing the appropriate boundary conditions.[2,10] For uniform excitation, the normal particle velocity on the transducer surface is independent of the position on the transducer, i.e., $v_o(\omega,\boldsymbol{r}_t)=v_o(\omega)$ where $\boldsymbol{r}_t$ is the vector traversing the transducer surface, and the velocity potential is expressed as

$$\Phi(\boldsymbol{r}_p,\omega)=v_0(\omega)\int_S \frac{e^{-jk|\boldsymbol{r}_p-\boldsymbol{r}_t|}}{2\pi|\boldsymbol{r}_p-\boldsymbol{r}_t|}\,dS \tag{1a}$$

$$=v_0(\omega)H(\boldsymbol{r}_p,k), \tag{1b}$$

where k is the wave number. The integral $H(\boldsymbol{r}_p,k)$ is the spatial transfer function of the transducer and is the subject of this paper.

In lossless media, k is a real valued quantity equal to ω/c_o, where c_o is the speed of sound. For a lossy medium, an imaginary component is introduced,

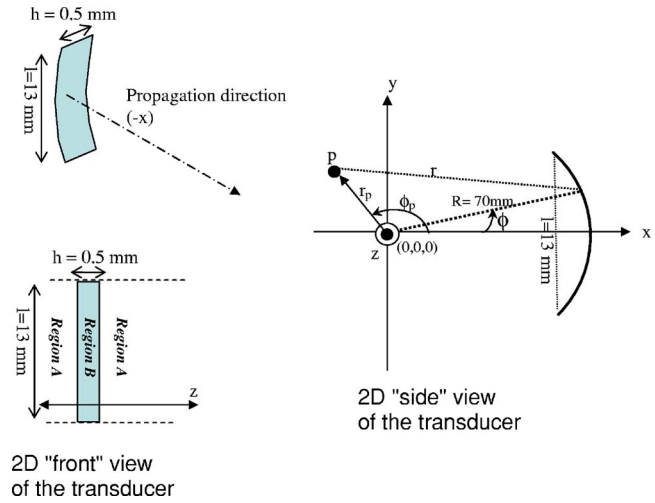

FIG. 1. (Color online) The geometry of the transducer and the coordinate system.

$$k(\omega)=\frac{\omega}{c_o(\omega)}-j\alpha(\omega), \tag{2}$$

where $\alpha(\omega)$ is the frequency dependent attenuation coefficient and $c_o(\omega)$ is the dispersive sound speed that is related to $\alpha(\omega)$ through causality. Closed form expressions for the causality relationship exist for power law attenuation as is appropriate for soft tissue.[11]

The pressure generated by the transducer at point $\boldsymbol{r}_p$ is calculated from Eq. (1a) as

$$p(\boldsymbol{r}_p,\omega)=-j\omega\rho_o\Phi(\boldsymbol{r}_p,\omega), \tag{3}$$

where ρ_o is the density.

III. SPATIAL TRANSFER FUNCTION FOR THE CYLINDRICAL GEOMETRY

For many commercial transducers, the source surface S is a truncated cylinder with lateral dimensions $l\times h$ and a radius R—see Fig. 1. The focal point of the cylindrical radiator is the origin of the cylindrical coordinates system, and the center of the element is at $(x=R,y=0,z=0)$, where the negative x direction is the principal propagation direction. The quantity r is the distance from a point on the transducer surface (R,ϕ,z) to the observation point $p(r_p,\phi_p,z_p)$. The spatial transfer function for this geometry is then

$$H(\boldsymbol{r}_p,k)=\int_S \frac{e^{-jkr}}{2\pi r}\,ds, \tag{4}$$

where S is the radiator surface and $ds=Rd\phi dz$. For transducer elements that are many wavelengths in size (as is typical for 1D ultrasound arrays), the kernel of Eq. (4) has a highly oscillatory behavior.

The semi-analytical method (SAM) we have developed to evaluate this oscillatory integral can be summarized as follows: First a change of variable is employed to smooth the oscillations of the kernel, which results in elliptical type integrals in terms of the angle ϕ. For most imaging transducers, ϕ is small (bounded by the half angle of the element) and the elliptical integrals can be approximated by quadratic

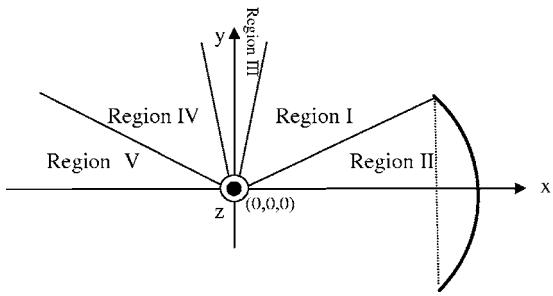

FIG. 2. Schematic showing the segmentation for ϕ_p.

type integrals for which closed form analytical solutions exist. The evaluation of ϕ integrals is carried out by dividing the $x-y$ plane into five regions (Fig. 2). Having reduced the dimension of the integral, the line integral kernels will be expanded as truncated series of Legendre polynomials, which can be integrated exactly term by term. The resulting spatial transfer function will be represented as summation of a small number of Bessel functions. In this section, the initial steps of our algorithm are introduced.

First the variable transformation is carried out by expressing the distance r in Eq. (4) in cylindrical coordinates as

$$r^2 = (r_p \cos(\phi_p) - R\cos(\phi))^2 + (r_p \sin(\phi_p) - R\sin(\phi))^2 + (z_p - z)^2 = M(\phi) + (z_p - z)^2, \tag{5}$$

where $M(\phi) = r_p^2 + R^2 - 2r_pR(\cos(\phi)\cos(\phi_p) + \sin(\phi)\sin(\phi_p))$ contains all the ϕ dependent terms. Equation (4) is written explicitly as

$$H(\boldsymbol{r}_p,k) = \frac{1}{2\pi}\int_{-\phi_H}^{\phi_H}\int_{-h/2}^{h/2}\frac{e^{-jk\sqrt{M(\phi)+(z_p-z)^2}}}{\sqrt{M(\phi)+(z_p-z)^2}}R\,dz\,d\phi, \tag{6}$$

where $\phi_H = \arcsin(l/2R)$ is the half-angle of the element in the elevation plane with respect to the geometrical focus.

First, to simplify the integral, the element $ds = Rd\phi dz$ is expressed as a function of r by eliminating the z dependence. Taking the derivative of both sides of Eq. (5),

$$dz = -\frac{r}{(z_p - z)}dr. \tag{7}$$

The sign of the element dz depends on the value of $z_p - z$ at the observation point. The field point z_p can have values between $[-\infty, \infty]$ but the surface point z is limited to the width of the transducer, h. Mathematically, $(z_p - z) = \sqrt{r^2 - M(\phi)}$ for $z_p > z$ and $-\sqrt{r^2 - M(\phi)}$ for $z_p < z$. Hence the new surface element ds is given as

$$ds = \pm\frac{r}{\sqrt{r^2 - M(\phi)}}Rd\phi dr \tag{8}$$

and the correct sign is determined from the observation point and will be discussed below.

The integral now takes the form

$$H(\boldsymbol{r}_p,k) = \frac{R}{2\pi}\int_{-\phi_H}^{\phi_H}\int_{F_1(\phi)}^{F_2(\phi)}E(r,\phi)\,dr\,d\phi, \tag{9}$$

where

$$E(r,\phi) = \frac{e^{-jkr}}{\sqrt{r^2 - M(\phi)}}. \tag{10}$$

The functions $F_1(\phi)$ and $F_2(\phi)$ will be discussed below.

The surface S is now a function of r and ϕ, and the new integration limits must be calculated. To express the new integrals, it is convenient to divide the half space in front of the transducer into two regions. Due to the symmetry in $x-y$ and $x-z$ planes of the radiator, the evaluation of $H(\boldsymbol{r}_p,k)$ can be restricted to one quadrant of the $y-z$ plane with $z_p \geq 0$ and $y \geq 0$. The two regions are defined as follows:

Region A ($z_p \geq h/2$): If $z_p > h/2$ (the maximum value of z), then $(z_p - z)$ will always be positive and $ds < 0$. The integral limits for r in Eq. (9) can be found by substituting the limiting values of z, $(-h/2, h/2)$ in Eq. (5), $F_1(\phi) = \sqrt{M(\phi) + (z_p - h/2)^2}$ and $F_2(\phi) = \sqrt{M(\phi) + (z_p + h/2)^2}$.

Region B ($0 \leq z_p < h/2$): If z_p is smaller than the limiting value of z, the integral needs to be segmented into two regions.

(i) If $-h/2 \leq z \leq z_p$, then $(z_p - z) \geq 0$ and $ds < 0$. Substituting the limiting values of z, $(-h/2, z_p)$, in Eq. (5), the integral limits in Eq. (9) are obtained as $F_1(\phi) = \sqrt{M(\phi)}$ and $F_2(\phi) = \sqrt{M(\phi) + (z_p + h/2)^2}$

(ii) If $z_p \leq z \leq h/2$, then $(z_p - z) \leq 0$ and $ds > 0$. The limiting values for z are $(z_p, h/2)$ and the new integral is defined with the limits $F_1(\phi) = \sqrt{M(\phi)}$ and $F_2(\phi) = \sqrt{M(\phi) + (z_p - h/2)^2}$

As a result, for this region SIR can be expressed as

$$H = \frac{R}{2\pi}\int_{-\phi_H}^{\phi_H}\left[\int_{\sqrt{M(\phi)}}^{\sqrt{M(\phi)+(z_p+h/2)^2}}E(r,\phi)\,dr + \int_{\sqrt{M(\phi)}}^{\sqrt{M(\phi)+(z_p-h/2)^2}}E(r,\phi)\,dr\right]d\phi. \tag{11}$$

All the integrals are of the form shown in Eq. (9) with the limits for the inner r integral given as

$$F_1(\phi) = \sqrt{M(\phi) + A_{zp}}, \tag{12a}$$

$$F_2(\phi) = \sqrt{M(\phi) + B_{zp}}; \tag{12b}$$

here A_{zp} and B_{zp} represent the region specific constants defined by the z_p value of the observation point.

IV. INTEGRAL EVALUATION

Equation (9) is an elliptical type integral (in terms of ϕ) and we were unable to find an analytical closed form solution. For most imaging transducers the ratio of $l/(2R)$ is small enough that $\cos(\phi)$ can be approximated with $(1 - \phi^2/2)$ and $\sin(\phi)$ with ϕ. For example, the parameters of the transducer used in this study are $R = 70$ mm and $l = 13$ mm, and $\phi = \arcsin\left(\frac{13}{140}\right) \simeq 5°$. By means of this smallness approximation, $M(\phi)$ can be described by

$$M(\phi) \approx (r_p^2 + R^2 - 2r_pR\cos(\phi_p)) - (2r_pR\sin(\phi_p))\phi + (r_pR\cos(\phi_p))\phi^2. \tag{13}$$

Employing the smallness approximation converts the elliptical integral in Eq. (9) into a quadratic type with respect to ϕ, which has a closed form solution. Therefore, it is necessary to change the order of integration so that the ϕ integral can be calculated. For observation points on the z axis ($r_p=0$) the kernel is independent of ϕ and this transformation cannot be employed. Therefore, the points on the z axis will be handled separately.

For the change of integration the $x-y$ plane is divided into five regions as shown in Fig. 2. Regions II and V correspond to the points inside the cone subtended by the circular boundary of the transducer and its center of curvature. Regions I and IV correspond to the points outside the ray cone, except for a small cone around the y axis, region III. For points close to the y axis, where $\cos(\phi_p)\rightarrow 0$, the coefficient of ϕ^2 in Eq. (13) becomes infinitesimally small and in subsequent steps results in numerical instability. In region III, $\cos(\phi)$ was approximated as unity and the last term in Eq. (13), with the troublesome $\cos(\phi_p)$ term, was dropped. To minimize the error arising from this approximation, a threshold value for ϕ_p was chosen such that $2r_pR\sin(\phi_p)\phi_H) > 10^3(r_pR\cos(\phi_p)\phi_H^2$. For the type of transducer used in this study, this threshold value, ϕ_t, was $69\pi/140$ and region III was defined between $69\pi/140$ and $(\pi-\phi_t)=71\pi/140$, which was the symmetric interval with respect to the y axis.

The underlying principle to convert Eq. (9) into line integrals is very similar for all the regions. In this paper, the mathematical details for regions I, II, and III are described. The introduced algebra covers all the mathematical tools needed to obtain the response at any observation point in front of the radiator. The interested reader is referred to Ref. 12 for the mathematical derivations of regions IV and V. The formulas for the spatial transfer functions for all regions are summarized in the Appendix.

A. Case 1: regions I and II $0\leq\phi_p\leq\phi_t$

In regions I and II, $M(\phi)$, $F_1(\phi)$ and $F_2(\phi)$ are represented by

$$M(\phi)\approx(r_p^2+R^2-2r_pR\cos(\phi_p))-(2r_pR\sin(\phi_p))\phi + (r_pR\cos(\phi_p))\phi^2 \tag{14a}$$

$$=a+b\phi+c\phi^2, \tag{14b}$$

$$F_1(\phi)\approx\sqrt{a+b\phi+c\phi^2+A_{zp}}, \tag{14c}$$

$$F_2(\phi)\approx\sqrt{a+b\phi+c\phi^2+B_{zp}}, \tag{14d}$$

where, to simplify the notation, the equations will be represented in terms of a, b, and c throughout this section. We will first introduce the solution for region I, as it sets the basis for the other solutions. The boundaries between the regions are described in terms of $\tan\phi_p$ and the reasoning behind this choice will be explained in the next section.

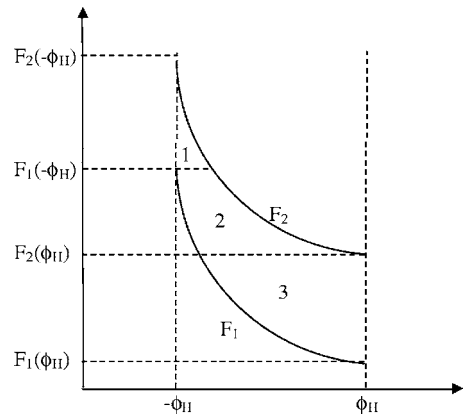

FIG. 3. The limit functions with monotonic decreasing dependence on ϕ.

1. Region I: $\phi_H<\tan\phi_p\leq\tan(\phi_t)$

The region of integration is shown in Fig. 3 and, to facilitate the change of order, it was necessary to divide the integral into three pieces (labeled as 1, 2, and 3 in Fig. 3):

$$\begin{aligned}\int_{-\phi_H}^{\phi_H}\int_{F_1(\phi)}^{F_2(\phi)}E(r,\phi)\,dr\,d\phi &= \int_{F_1(-\phi_H)}^{F_2(-\phi_H)}\int_{(-\phi_H)}^{F_2^{-1}(r)}E(r,\phi)\,d\phi\,dr \\ &+\int_{F_2(\phi_H)}^{F_1(-\phi_H)}\int_{F_1^{-1}(r)}^{F_2^{-1}(r)}E(r,\phi)\,d\phi\,dr \\ &+\int_{F_1(\phi_H)}^{F_2(\phi_H)}\int_{F_1^{-1}(r)}^{\phi_H}E(r,\phi)\,d\phi\,dr.\end{aligned} \tag{15}$$

The mapping functions from r to ϕ, which are denoted with $F_1^{-1}(r)$ and $F_2^{-1}(r)$, are not single valued, e.g., $F_1(\phi)=\sqrt{a+b\phi+c\phi^2+A_{zp}}$, which is a quadratic with two roots. To solve the problem uniquely, the correct root must be picked and this motivates the separation into regions. The derivative of the quadratic term changes sign at $-b/2c=\tan(\phi_p)$. Hence, the boundaries between the regions are described in terms of $\tan(\phi_p)$. For region I, $\tan(\phi_p)>\phi_H$ and the appropriate results are

$$F_1^{-1}(r)=\phi=\frac{-b-\sqrt{b^2-4c(a+A_{zp}-r^2)}}{2c}, \tag{16a}$$

$$F_2^{-1}(r)=\phi=\frac{-b-\sqrt{b^2-4c(a+B_{zp}-r^2)}}{2c}. \tag{16b}$$

Moreover, in this region, $c>0$ and the integral with respect to ϕ is given as[13]

$$\int\frac{1}{\sqrt{r^2-(a+b\phi+c\phi^2)}}\,d\phi=\frac{1}{\sqrt{c}}\arcsin\left(\frac{-2c\phi-b}{\sqrt{b^2+4c(r^2-a)}}\right), \tag{17}$$

hence Eq. (15) can now be written as

$$\int_{-\phi_H}^{\phi_H}\int_{F_1(\phi)}^{F_2(\phi)} E(r,\phi)\,dr\,d\phi$$
$$= \int_{F_1(-\phi_H)}^{F_2(-\phi_H)} e^{-jkr}[\Psi_2(r)-\Psi_3(r)]\,dr$$
$$+ \int_{F_2(\phi_H)}^{F_1(-\phi_H)} e^{-jkr}[\Psi_2(r)-\Psi_1(r)]\,dr + \int_{F_1(\phi_H)}^{F_2(\phi_H)}$$
$$\times e^{-jkr}[\Psi_4(r)-\Psi_1(r)]\,dr, \tag{18}$$

where

$$\Psi_1(r) = -\frac{1}{\sqrt{c}}\arcsin\left(\sqrt{1-\frac{4cA_{zp}}{b^2+4r^2c-4ac}}\right), \tag{19a}$$

$$\Psi_2(r) = -\frac{1}{\sqrt{c}}\arcsin\left(\sqrt{1-\frac{4cB_{zp}}{b^2+4r^2c-4ac}}\right), \tag{19b}$$

$$\Psi_3(r) = -\frac{1}{\sqrt{c}}\arcsin\left(\sqrt{\frac{2c\phi_H-b}{\sqrt{b^2+4r^2c-4ac}}}\right), \tag{19c}$$

$$\Psi_4(r) = -\frac{1}{\sqrt{c}}\arcsin\left(\sqrt{\frac{-2c\phi_H-b}{\sqrt{b^2+4r^2c-4ac}}}\right). \tag{19d}$$

The transfer function in a compact form consists of four line integrals:

$$H = \frac{R}{2\pi}\left[\int_{F_1(\phi_H)}^{F_1(-\phi_H)} e^{-jkr}[-\Psi_1(r)]\,dr + \int_{F_2(\phi_H)}^{F_2(-\phi_H)} e^{-jkr}[\Psi_2(r)]\,dr + \int_{F_1(-\phi_H)}^{F_2(-\phi_H)} e^{-jkr} \times[-\Psi_3(r)]\,dr + \int_{F_1(\phi_H)}^{F_2(\phi_H)} e^{-jkr}[\Psi_4(r)]\,dr\right]. \tag{20}$$

2. Region II: $\tan\phi_p \le \phi_H$

When $\tan(\phi_p)$ is smaller than the limiting value of ϕ, the inverse mapping functions $F_1^{-1}(r)$ and $F_2^{-1}(r)$ change sign in the integral interval. Therefore, the integral in Eq. (9) should be decomposed into two parts for a unique representation:

$$\int_{-\phi_H}^{\phi_H}\int_{F_1(\phi)}^{F_2(\phi)} E(r,\phi)\,dr\,d\phi = H_1 + H_2 + \int_{-\phi_H}^{\tan(\phi_p)}\int_{F_1(\phi)}^{F_2(\phi)} E(r,\phi)\,dr\,d\phi + \int_{\tan(\phi_p)}^{\phi_H}\int_{F_1(\phi)}^{F_2(\phi)} E(r,\phi)\,dr\,d\phi. \tag{21}$$

To obtain H_1, the algorithm used in region I will be implemented. The limit functions $F_1(\phi)$ and $F_2(\phi)$ are decreasing functions of ϕ and the inverses of the functions are represented with the negative roots, hence the resulting integral

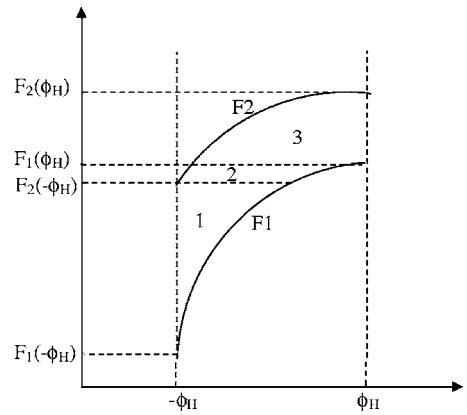

FIG. 4. The limit functions with monotonic increasing dependence on ϕ.

has a form similar to the previous case and can be expressed as

$$H_1 = \frac{R}{2\pi}\left[\int_{F_1(\phi_1)}^{F_1(-\phi_H)} e^{-jkr}[-\Psi_1(r)]\,dr + \int_{F_2(\phi_1)}^{F_2(-\phi_H)} e^{-jkr}[\Psi_2(r)]\,dr + \int_{F_1(-\phi_H)}^{F_2(-\phi_H)} e^{-jkr} \times[-\Psi_3(r)]\,dr\right] \tag{22}$$

where $\phi_1 = \tan(\phi_p)$ and the $\Psi_4(r)$ integral vanishes in this interval.

To calculate H_2, the same path will be followed with minor modifications. For this case, M and r are the increasing functions of ϕ. The behavior of the limiting functions with respect to ϕ is given in Fig. 4. After algebraic manipulations, the resulting integral can be written as

$$H_2 = \frac{R}{2\pi}\left[\int_{F_1(\phi_1)}^{F_1(\phi_H)} e^{-jkr}[-\Psi_1(r)]\,dr + \int_{F_2(\phi_1)}^{F_2(\phi_H)} e^{-jkr}[\Psi_2(r)]\,dr + \int_{F_1(\phi_H)}^{F_2(\phi_H)} e^{-jkr}[\Psi_4(r)]\,dr\right] \tag{23}$$

and the $\Psi_3(r)$ integrals vanishes in this interval.

B. Case 2: region III, $\phi_t < \phi_p \le \pi - \phi_t$

As discussed previously, the approximation $\cos(\phi) \approx 1$ is employed in this region, which is equivalent to setting $c = 0$ in Eq. (14a). The integral is divided up into three pieces as was done for region I [Eq. (15)], where the mapping functions are now

$$F_1^{-1}(r) = \frac{r^2 - a - A_{zp}}{b}, \tag{24a}$$

$$F_2^{-1}(r) = \frac{r^2 - a - B_{zp}}{b}. \tag{24b}$$

The ϕ integrals can be evaluated as follows,

$$\int \frac{1}{\sqrt{r^2-(a+b\phi)}}\,d\phi = \frac{2\sqrt{r^2-(a+b\phi)}}{-b}, \tag{25}$$

and the spatial transfer function for region III is

$$H = \frac{R}{\pi(-b)}\left\{\int_{F_1(-\phi_H)}^{F_2(-\phi_H)} e^{-jkr}[\sqrt{B_{zp}}-\sqrt{r^2-(a-b\phi_H)}]\,dr + \int_{F_2(\phi_H)}^{F_1(-\phi_H)} e^{-jkr}[\sqrt{B_{zp}}-\sqrt{A_{zp}}]\,dr + \int_{F_1(\phi_H)}^{F_2(\phi_H)} e^{-jkr}[\sqrt{r^2-(a+b\phi_H)}-\sqrt{A_{zp}}]\,dr\right\}, \tag{26}$$

with the definitions

$$\Psi_5(r) = \sqrt{r^2-(a-b\phi_H)}, \tag{27a}$$

$$\Psi_6(r) = \sqrt{r^2-(a+b\phi_H)}. \tag{27b}$$

The spatial transfer function is expressed in a compact form as

$$H = \frac{R}{\pi(-b)}\left[\int_{F_2(\phi_H)}^{F_2(-\phi_H)} e^{-jkr}[\sqrt{B_{zp}}]\,dr + \int_{F_1(-\phi_H)}^{F_2(-\phi_H)} e^{-jkr} \times[-\Psi_5(r)]\,dr + \int_{F_1(\phi_H)}^{F_2(\phi_H)} e^{-jkr}[\Psi_6(r)]\,dr + \int_{F_1(\phi_H)}^{F_1(-\phi_H)} e^{-jkr}[-\sqrt{A_{zp}}]\,dr\right]. \tag{28}$$

C. Case 3: on the *z* axis $r_p=0$

For this case, Eq. (9) is written as

$$H = \frac{R}{2\pi}\int_{-\phi_H}^{\phi_H}\int_{F_1}^{F_2} \frac{e^{-jkr}}{\sqrt{r^2-M}}\,dr\,d\phi, \tag{29}$$

where $M=R^2$ for $r_p=0$, and F_1 and F_2 reduce to $\sqrt{R^2+(z_p\pm h/2)^2}$ where the sign depends on the region. The integrand is independent of ϕ and Eq. (29) is expressed as

$$H = \frac{R\phi_H}{\pi}\int_{F_1}^{F_2} \frac{e^{-jkr}}{\sqrt{r^2-R^2}}\,dr. \tag{30}$$

To remove the singularity caused by $F_1=R$, the integration by parts is employed and Eq. (30) is rewritten as

$$H = \frac{R\phi_H}{\pi}\left[e^{-jkr}\ln(r+\sqrt{r^2-R^2})\Big|_{F_1}^{F_2} - \int_{F_1}^{F_2}(-jk)e^{-jkr}\ln(r+\sqrt{r^2-R^2})\,dr\right]. \tag{31}$$

D. Polynomial approximation

The compact expressions for the spatial transfer function of the cylindrical radiator involve line integrals, most of which cannot be computed analytically. The integrals with the nonlinear functions of r can be evaluated using a numerical integration technique such as Gauss quadrature. The drawback of such a time consuming implementation is that a separate numerical integral routine must be used for each different frequency value.

In this study, a faster approach is introduced. The integrands were expanded as a series of Legendre polynomials. The Legendre polynomials were chosen as the expansion basis functions since the coefficients of the resulting series can be obtained without an integration routine and a closed form solution exists for the exponential integrands found in the expressions here. The resulting spatial transfer function is represented as summation of a small number of Bessel functions.

The normalized Legendre polynomials $\bar{P}_n(x)$ form a complete orthogonal system over the interval $[-1,1]$. Therefore function $f(x)$ defined in this interval may be expanded in terms of the normalized Legendre polynomials as

$$f(x) = \sum_{n=0}^{n=\infty} a_n\bar{P}_n(x), \tag{32a}$$

where the coefficients a_n are obtained from

$$a_n = \int_{-1}^{1} \bar{P}_n(x)f(x)\,dx. \tag{32b}$$

If $f(x)$ is smooth and well behaved, it can be represented with a truncated series where the upper limit of Eq. (32a) is replaced with N.

It can be shown that the coefficients of the truncated Legendre series are given by[14]

$$a_n = \sum_{q=1}^{n+1} W_q\bar{P}_n(\lambda_q)f(\lambda_q), \tag{33}$$

where λ_q are the zeros of the Legendre polynomial of order $N+1$ and W_q are the weights of the Gauss-Legendre quadrature, that is, the coefficients a_n can be obtained without integration.

The application of this series expansion to our algorithm will be as follows. As a general representation, the integrals that one needs to compute can be written as

$$\int_a^b e^{-jkr}\Psi(r)\,dr = Ae^{-jkB}\int_{-1}^{1} e^{-jkAx}\Psi(Ax+B)\,dx \tag{34}$$

with $r=Ax+B$, $A=(b-a)/2$, and $B=(b+a)/2$. The function $\Psi(Ax+B)$ is expanded in terms of the Legendre polynomials

$$\Psi(Ax+B) = \sum_{n=0}^{n=N} a_n\bar{P}_n(x), \tag{35a}$$

and, using the identity[15] [p. 649]

$$\int_{-1}^{1} e^{-jkx}\bar{P}_n(x)\,dx = \sqrt{4n+2}(j)^{-n}j_n(k), \tag{35b}$$

where $j_n(k)$ is the nth order spherical Bessel function, one obtains

$$\int_a^b e^{-jkr}\Psi(r)\,dr = Ae^{-jkB}\sum_{n=0}^{N} a_n\sqrt{4n+2}(j)^{-n}j_n(Ak). \quad (35c)$$

The resulting summation, Eq. (35c), is valid for any wave number and can be used to evaluate the remaining integrals in Eqs. (20), (22), (23), (28), and (31). From these one can predict the acoustic fields in both lossless and attenuating media.

V. RESULTS

We carried out numerical experiments to verify the SAM introduced in this paper. Using the formulas given in Sec. IV, the spatial transfer function of a cylindrical transducer was calculated and compared with the results of direct numerical integration of Eq. (6) using a brute force quadrature routine. The SAM was also compared to Field II and the Fresnel approximation along the axis of the element and performance analysis is given. The element had lateral dimensions 13×0.5 mm^2, a 70-mm elevation focal length, and a center frequency of 3.5 MHz and was based on a clinical probe (Model 8665, BK Medical, Wilmington, MA). To have a reasonable sized problem the maximum frequency of the signals was limited to 10 MHz.

A. Direct numerical approach (DNA)

A number of direct numerical integration techniques were applied to compute Eq. (6). The Gauss-Legendre quadrature was found to produce the most accurate results in the shortest time compared to other standard integration techniques such as the trapezoidal rule and Simpson's rule.

The 2D numerical routine can be summarized with the following equation:

$$H \simeq \frac{R}{2\pi}\sum_{n=1}^{\bar{N}}\sum_{u=1}^{\bar{U}} w_n w_u \frac{e^{-jk\sqrt{M(\phi_n)+(z_p-z_u)^2}}}{\sqrt{M(\phi_n)+(z_p-z_u)^2}}, \quad (36)$$

where ϕ_n and z_u denote the abscissas, and w_n, w_u are the weights for ϕ and z, respectively. The number of terms is determined according to the maximum frequency component of the signal. In this study, 2π terms per minimum wavelength were found to be sufficient for an accurate integral evaluation. The number of terms for z was $\bar{U}$ $=\text{round}(2\pi f_{\max}h/c_o)$ and the number of terms for ϕ was $\bar{N}=\text{round}(2R\phi_H\bar{U}/h)$. The routine was implemented in Matlab R14 on a Pentium 4, 3 GHz, 1 GB RAM machine. For the transducer used in this study $\bar{N}=547$ and $\bar{U}=21$.

B. Comparison of SAM and DNA

A number of numerical experiments were performed to evaluate the performance of our method. In this study, four comparison results are presented. Figures 5–7 each show contour plots of the envelope of the normalized wave forms for two cases: (a) the simulated response calculated with the semi-analytical method (SAM) introduced in Sec. IV and (b) the simulated response computed with the direct numerical approach (DNA) in Sec. V A without any approximations. The error between the two simulated responses [(a) and (b)] and the speed improvement in computation time are the most important parameters to assess the performance of our method. The measures that will be used to compare these two results are defined as follows:

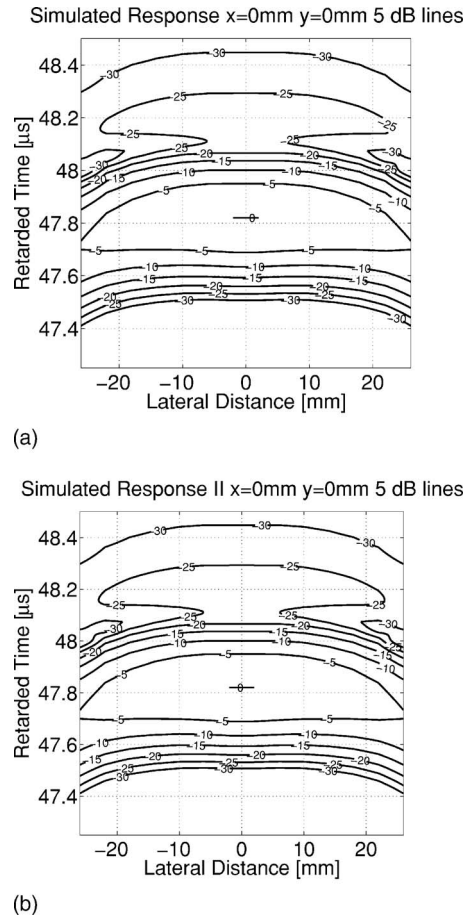

FIG. 5. Amplitude of envelope of acoustic field at $x=0$ and $y=0$ mm. (a) Fast semi-analytical technique. (b) Direct computational method. Contours are at 5-dB intervals. Retarded time scale: $t_r=t-r^2/(2Rc_0)$.

$$\text{Error }\% = 100\frac{\|\text{SAM}-\text{DNA}\|_2}{\|\text{DNA}\|_2}, \quad (37a)$$

$$\text{Speed Improvement Ratio} = \frac{\text{Total time required to compute DNA}}{\text{Total time required to compute SAM}}. \quad (37b)$$

The real valued wave number used in these simulations was equal to ω/c_o, where $c_o=1500$ m/s.

Figure 5 compares the field predictions in the scan plane (z axis) of the transducer element at the elevation focus. In this case, 14 equally spaced observation points are chosen between −26 and 26 mm. The time axis was adjusted to remove the curvature of the wavefronts associated with spreading from the element. This allows for a detailed comparison of the phase fronts. The error between the two simulated responses was $7.5\times 10^{-5}\%$ and the speed improvement ratio 1355. The total time required to compute SAM was 0.3 s.

In Fig. 6, the off-axis propagation in regions I and II was investigated where the approximation for ϕ had the most significant effect on the results. For this experiment, the ob-

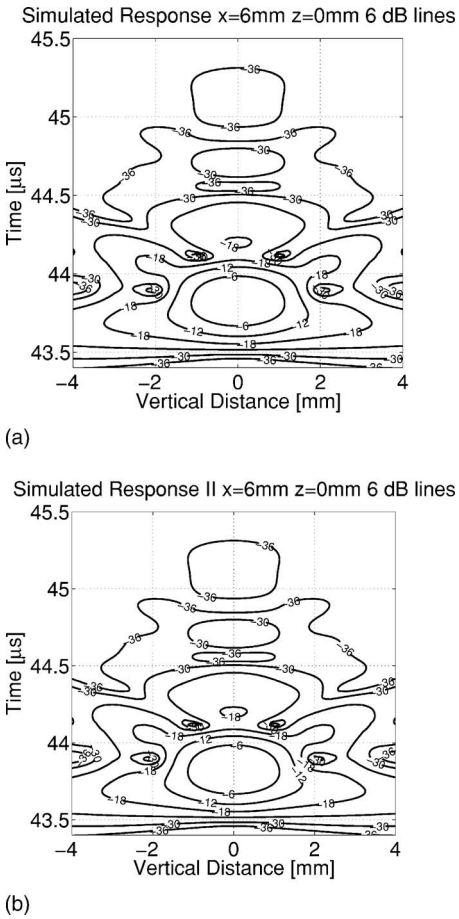

FIG. 6. Amplitude of envelope of acoustic field at $x=6$ and $z=0$ mm. (a) Fast semi-analytical technique. (b) Direct computational method. Contours are at 6-dB intervals.

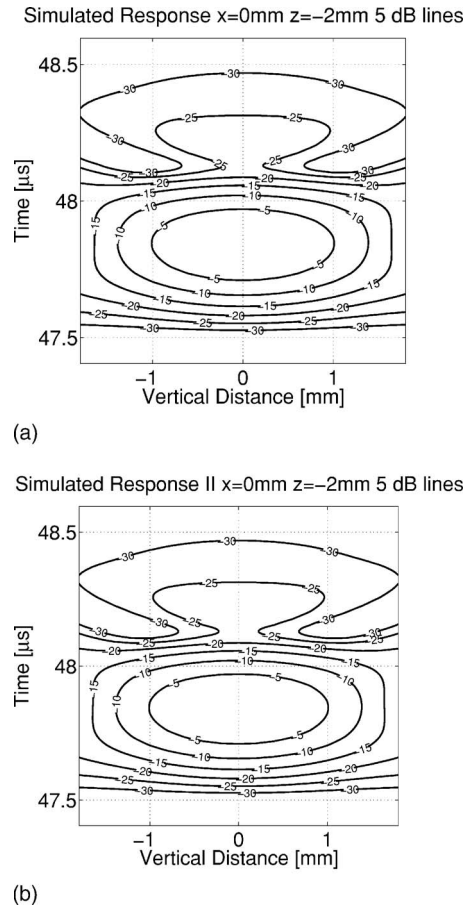

FIG. 7. Amplitude of envelope of acoustic field at $x=0$ and $z=-2$ mm. (a) Fast semi-analytical technique. (b) Direct computational method. Contours are at 5-dB intervals.

servation points were 6 mm behind the focus and parallel to the y axis. Forty-one equally spaced points were selected between −4 and 4 mm. The error was found to be 0.12% and the speed improvement ratio 225 times. The total time required to compute the SAM was 3.3 s.

Figure 7 shows the acoustic field in region III, on the y axis, for $z_p=-2$ mm. The observation points were selected at 19 equally spaced locations between −1.8 and 1.8 mm. For this region, the error between two simulated responses [(a) and (b)] was found to be 0.07% and the speed improvement ratio 541. The total time required to compute the SAM was 0.7 s.

The numerical results presented here were also validated with experimental measurements on the field from a single element of the clinical probe. There was a good agreement confirming that the small half-angle approximation was appropriate for this transducer. The interested reader is referred to Ref. 12 for the comparison results.

C. Attenuating media

A numerical experiment was performed to assess the performance of the method in lossy media. The same experiment described in Fig. 6 was simulated with a complex wave number representing a power law attenuating medium. Attenuation was incorporated into the model by using $\alpha_b = 54(\omega/2\pi 3.5\ \text{MHz})^{1.2}$ Np/m [which corresponds to $4.7(\omega/2\pi 3.5\ \text{MHz})^{1.2}$ dB/cm] and is appropriate for tissue.[12] The wave number was defined as

$$k^2(\omega) = \frac{\omega^2}{c_o^2} - j\frac{2\omega\alpha_b(\omega)}{c_o}. \tag{38}$$

The predicted responses obtained with the two different methods are given in Fig. 8. There is an excellent agreement between two results. Quantitatively, the speed improvement ratio is obtained as 225 times and the error between two simulations is 0.08%. The total time required to compute the SAM was 3.6 s.

D. Comparison with Field II and the Fresnel approximation

A numerical experiment was performed to compare the performance of the SAM, with the Field II program and calculations based on the Fresnel approximation. The subroutine "xdc_focused_array" was used from the Field II package with following parameters: no_elements =1, width $=5\times 10^{-4}$, height =0.013, kerf $=1.6667\times 10^{-4}$, Rfocus =0.07, no_sub_x =1, no_sub_y =200, and focus =[0 0 0.07]. The Fresnel approximation was implemented in Matlab 6.0.0.88 (R12) using the formula given in Ref. 6 (p. 157, Eq. 6.27b).

Figure 9 shows two plots of the amplitude of the 3.5-MHz component of a pulse as a function of distance along

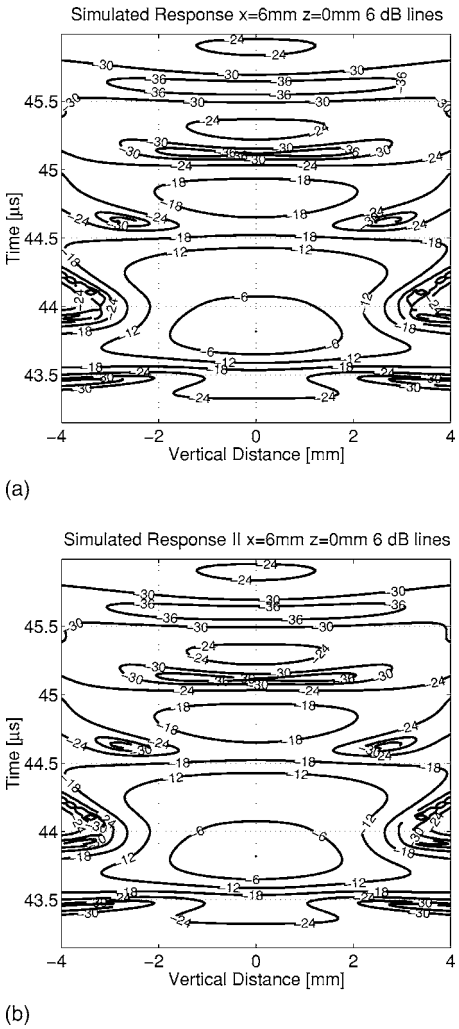

FIG. 8. Amplitude of envelope of acoustic field in lossy medium at $x=6$ and $z=0$ mm. (a) Fast semi-analytical technique. (b) Direct computational method. Contours are at 6-dB intervals.

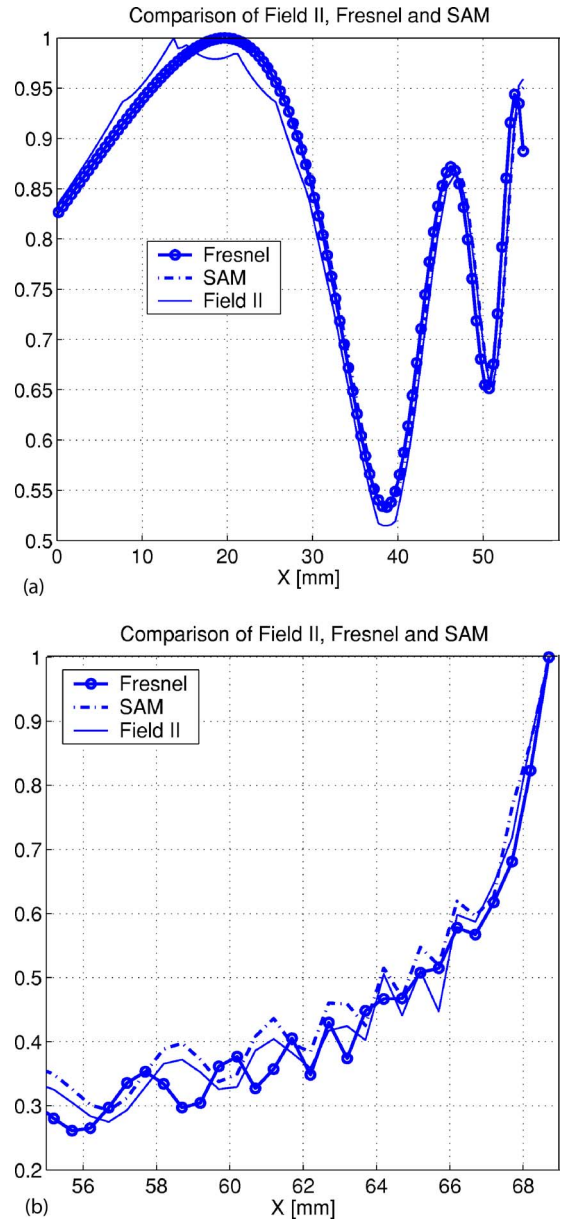

FIG. 9. (Color online) Prediction of the amplitude of the 3.5-MHz component along the axis of the transducer. Comparison of Field II, Fresnel, and SAM.

axis of the element from 0 to 69 mm in 0.5-mm steps. One can see that around the focus of the transducer [Fig. 9(a)] the Fresnel approximation gives an accurate result. However, in the near field [Fig. 9(b)] the paraxial approximation fails to capture the oscillations in the pressure field accurately. In comparison Field II provides accurate results in the near field while showing some discrepancy in the focal region. This is consistent with reports that the SIR employed by Field II can be inefficient in the focal region.[4]

Table I shows a comparison of the total computation time and the estimated error relative to the DNA for Field II, Fresnel, and SAM on a computer with a Pentium 4, 1.6 GHz and 768 MB RAM. It can be seen that the SAM is more accurate than the Fresnel or Field II methods. The Fresnel method was the fastest, as would be expected due to its use of the paraxial approximation. The Field II program appears faster than the SAM, however the bulk of the computations in Field II are carried out in a compiled C-file (Matlab "mex" file), which is inherently faster than the direct Matlab implementation of the SAM (and the Fresnel method). A direct C-implementation of the SAM should lead to at least an order of magnitude improvement in speed, making it equivalent to Field II, and could potentially be another order of magnitude faster.

VI. CONCLUSION

In this study, a fast method to compute the spatial transfer function of cylindrically concave transducers in lossless

TABLE I. Comparison of Field II, Fresnel, and SAM.

Figure 9(a)	SAM	Fresnel	Field II
Error (%)	0.08	2.10	2.4
Computation time (s)	4.05	0.33	0.22
Figure 9(b)			
Error (%)	1.07	10.58	5.73
Computation time (s)	1.22	0.08	0.22

and attenuating medium was introduced. For cylindrically focused transducers, with small half-angles in the elevation plane, the 2D surface integral was transformed from an elliptic type to a parabolic type. The integrals could be evaluated by reducing the problem to a 1D line integral. The remaining integrand was expressed as a truncated series of Legendre polynomials, from which it was possible to evaluate the line integral as a sum of spherical Bessel functions. The form of the line integrals is such that the coefficients of the Legendre polynomials depend only on geometry and not on frequency. They only need to be calculated once for specific elements and then the response at any frequency can be determined by a summation where the number of terms does not depend on frequency. This contrasts to direct integration approaches, which need to employ finer discretization for higher frequency components.

The method was compared to an optimized numerical method, which evaluated the surface integral directly. The speed of the new algorithm depends on the number of line integrals that need to be evaluated for an observation point. For the specific transducer used in this study, the speed improvement was between 40 and 1400 and the maximum error between two simulations was found to be 0.4%. The semi-analytical frequency domain method can predict the spatial transfer function of a cylindrical radiator in lossy medium simply by adding an imaginary component to the wave number.

In summary, a powerful semi-analytical method has been presented that complements the numerical approaches in the current literature. The approach can predict the acoustic field for a cylindrical concave transducer in attenuating homogeneous media. The approach can be applied to determine the fields in classical beam forming and also for applications such as tomography, which do not employ delay and sum beamforming.

ACKNOWLEDGMENTS

This work was supported in part by CenSSIS (the Center for Subsurface Sensing and Imaging Systems), under the Engineering Research Centers Program of the National Science Foundation (Award No. EEC-9986821). The authors are grateful for technical assistance provided by Dr. Emmanuel Bossy and Ersel Karbeyaz.

APPENDIX: ACOUSTIC FIELD OF A CYLINDRICALLY CONCAVE TRANSDUCER

The type of the integral to be solved here can be expressed in the following form:

$$\frac{R}{2\pi}\int_{-\phi_H}^{\phi_H}\int_{F_1(\phi)}^{F_2(\phi)}\frac{e^{-jkr}}{\sqrt{r^2-M(\phi)}}\,dr\,d\phi, \tag{A1a}$$

where

$$F_1(\phi)=\sqrt{M(\phi)+A_{zp}}, \tag{A1b}$$

$$F_2(\phi)=\sqrt{M(\phi)+B_{zp}}, \tag{A1c}$$

$$M(\phi)=r_p^2+R^2-2r_pR\cos(\phi-\phi_p), \tag{A1d}$$

where A_{zp} and B_{zp} represent the region specific constants defined by the z_p value of the observation point.

1. Case 1: Regions I and II $0\le\phi_p\le\phi_t$

In this region $M(\phi)$, $F_1(\phi)$, and $F_2(\phi)$ are represented by

$$M(\phi)\approx(r_p^2+R^2-2r_pR\cos(\phi_p))-(2r_pR\sin(\phi_p))\phi \tag{A2a}$$

$$+(r_pR\cos(\phi_p))\phi^2 \tag{A2b}$$

$$=a+b\phi+c\phi^2, \tag{A2c}$$

$$F_1(\phi)\approx\sqrt{a+b\phi+c\phi^2+A_{zp}}, \tag{A2d}$$

$$F_2(\phi)\approx\sqrt{a+b\phi+c\phi^2+B_{zp}}. \tag{A2e}$$

a. Region I: $\phi_H<\tan\phi_p\le\tan(\phi_t)$

The expression for the spatial transfer function is given by

$$H=\frac{R}{2\pi}\left[\int_{F_1(\phi_H)}^{F_1(-\phi_H)}e^{-jkr}[-\Psi_1(r)]\,dr+\int_{F_2(\phi_H)}^{F_2(-\phi_H)}e^{-jkr}[\Psi_2(r)]\,dr+\int_{F_1(-\phi_H)}^{F_2(-\phi_H)}e^{-jkr}\times[-\Psi_3(r)]\,dr+\int_{F_1(\phi_H)}^{F_2(\phi_H)}e^{-jkr}[\Psi_4(r)]\,dr\right], \tag{A3}$$

where

$$\Psi_1(r)=-\frac{1}{\sqrt{c}}\arcsin\left(\sqrt{1-\frac{4cA_{zp}}{b^2+4r^2c-4ac}}\right), \tag{A4a}$$

$$\Psi_2(r)=-\frac{1}{\sqrt{c}}\arcsin\left(\sqrt{1-\frac{4cB_{zp}}{b^2+4r^2c-4ac}}\right), \tag{A4b}$$

$$\Psi_3(r)=-\frac{1}{\sqrt{c}}\arcsin\left(\frac{2c\phi_H-b}{\sqrt{b^2+4r^2c-4ac}}\right), \tag{A4c}$$

$$\Psi_4(r)=-\frac{1}{\sqrt{c}}\arcsin\left(\frac{-2c\phi_H-b}{\sqrt{b^2+4r^2c-4ac}}\right). \tag{A4d}$$

b. Region II: $\tan\phi_p\le\phi_H$

The expression is given as the summation of the two responses:

$$\int_{-\phi_H}^{\phi_H}\int_{F_1(\phi)}^{F_2(\phi)}dr\,d\phi=H_1+H_2. \tag{A5}$$

H_1:

$$H_1 = \frac{R}{2\pi}\left[\int_{F_1(\phi_1)}^{F_1(-\phi_H)} e^{-jkr}[-\Psi_1(r)]\,dr + \int_{F_2(\phi_1)}^{F_2(-\phi_H)} e^{-jkr}[\Psi_2(r)]\,dr + \int_{F_1(-\phi_H)}^{F_2(-\phi_H)} e^{-jkr}[\Psi_3(r)]\,dr\right], \tag{A6}$$

where

$$\phi_1 = \tan(\phi_p). \tag{A7a}$$

H_2:

$$H_2 = \frac{R}{2\pi}\left[\int_{F_1(\phi_1)}^{F_1(\phi_H)} e^{-jkr}[-\Psi_1(r)]\,dr + \int_{F_2(\phi_1)}^{F_2(\phi_H)} e^{-jkr}[\Psi_2(r)]\,dr + \int_{F_1(\phi_H)}^{F_2(\phi_H)} e^{-jkr}[\Psi_4(r)]\,dr\right]. \tag{A8}$$

2. Case 2: Region III, $\phi_t < \phi_p \leq \pi - \phi_t$

$$H = \frac{R}{\pi(-b)}\left[\int_{F_2(\phi_H)}^{F_2(-\phi_H)} e^{-jkr}[\sqrt{B_{zp}}]\,dr + \int_{F_1(-\phi_H)}^{F_2(-\phi_H)} e^{-jkr} \times[-\Psi_5(r)]\,dr + \int_{F_1(\phi_H)}^{F_2(\phi_H)} e^{-jkr}[\Psi_6(r)]\,dr + \int_{F_1(\phi_H)}^{F_1(-\phi_H)} e^{-jkr}[-\sqrt{A_{zp}}]\right], \tag{A9}$$

where

$$\Psi_5(r) = \sqrt{r^2 - (a - b\phi_H)}, \tag{A10a}$$

$$\Psi_6(r) = \sqrt{r^2 - (a + b\phi_H)}, \tag{A10b}$$

$$F_1(\phi) = \sqrt{a + b\phi + A_{zp}}, \tag{A10c}$$

$$F_2(\phi) = \sqrt{a + b\phi + B_{zp}}. \tag{A10d}$$

3. Case 3: Regions IV and V $\pi - \phi_t \leq \phi_p \leq \pi$

$M(\phi)$, $F_1(\phi)$, and $F_2(\phi)$ have the same forms in Sec. IV A as

$$M(\phi) \approx (r_p^2 + R^2 - 2r_pR\cos(\phi_p)) - (2r_pR\sin(\phi_p))\phi \tag{A11a}$$

$$+ (r_pR\cos(\phi_p))\phi^2 \tag{A11b}$$

$$= a + b\phi + c\phi^2, \tag{A11c}$$

$$F_1(\phi) \approx \sqrt{a + b\phi + c\phi^2 + A_{zp}}, \tag{A11d}$$

$$F_2(\phi) \approx \sqrt{a + b\phi + c\phi^2 + B_{zp}}. \tag{A11e}$$

a. Region IV: $\tan\phi_p < -\phi_H$

$$H = \frac{R}{2\pi}\left[\int_{F_1(\phi_H)}^{F_1(-\phi_H)} e^{-jkr}[-\Psi_7(r)]\,dr + \int_{F_2(\phi_H)}^{F_2(-\phi_H)} e^{-jkr}[\Psi_8(r)]\,dr + \int_{F_1(-\phi_H)}^{F_2(-\phi_H)} e^{-jkr} \times[-\Psi_9(r)]\,dr + \int_{F_1(\phi_H)}^{F_2(\phi_H)} e^{-jkr}[\Psi_{10}(r)]\,dr\right], \tag{A12}$$

where

$$-\phi_H = -\arcsin(l/R), \tag{A13a}$$

$$\phi_H = \arcsin(l/R), \tag{A13b}$$

$$\Psi_7(r) = \frac{1}{\sqrt{-c}}\ln\left(2\sqrt{-cA_{zp}} + \sqrt{b^2 - 4c(a + A_{zp} - r^2)}\right), \tag{A13c}$$

$$\Psi_8(r) = \frac{1}{\sqrt{-c}}\ln\left(2\sqrt{-cB_{zp}} + \sqrt{b^2 - 4c(a + B_{zp} - r^2)}\right), \tag{A13d}$$

$$\Psi_9(r) = \frac{1}{\sqrt{-c}}\ln\left(2\sqrt{-c(r^2 - a + b\phi_H - c\phi_H^2)} + 2c\phi_H - b\right), \tag{A13e}$$

$$\Psi_{10}(r) = \frac{1}{\sqrt{-c}}\ln\left(2\sqrt{-c(r^2 - a + b\phi_H - c\phi_H^2)} - 2c\phi_H - b\right). \tag{A13f}$$

b. Region V: $\tan\phi_p \geq -\phi_H$

$$\int_{-\phi_H}^{\phi_H}\int_{F_1(\phi)}^{F_2(\phi)} dr\,d\phi = H_1 + H_2. \tag{A14}$$

H_1:

$$H_1 = \frac{R}{2\pi}\left[\int_{F_1^*(\phi_H)}^{F_1^*(\phi_2)} e^{-jkr}[-\Psi_7(r)]\,dr + \int_{F_2^*(\phi_H)}^{F_2^*(\phi_2)} e^{-jkr}[\Psi_8(r)]\,dr + \int_{F_1^*(\phi_2)}^{F_2^*(\phi_2)} e^{-jkr} \times[-\Psi_{11}(r)]\,dr + \int_{F_1^*(\phi_H)}^{F_2^*(\phi_H)} e^{-jkr}[\Psi_{12}(r)]\,dr\right], \tag{A15}$$

$$F_1^*(\phi^*) = \sqrt{(a - b\phi^* + c(\phi^*)^2 + A_{zp}}, \tag{A16a}$$

$$F_2^*(\phi^*) = \sqrt{(a - b\phi^* + c(\phi^*)^2 + B_{zp}}, \tag{A16b}$$

$$\Psi_{11}(r) = \frac{1}{\sqrt{-c}}\ln\left(2\sqrt{-c(r^2 - a + b\phi_2 - c\phi_2^2)} - 2c\phi_2 + b\right), \tag{A16c}$$

$$\Psi_{12}(r) = \frac{1}{\sqrt{-c}} \ln\left(2\sqrt{-c(r^2 - a + b\phi_H - c\phi_H^2)} - 2c\phi_H + b\right), \tag{A16d}$$

$$\phi_2 = -\tan(\phi_p). \tag{A16e}$$

H_2:

$$H_2 = \frac{R}{2\pi}\left[\int_{F_1(\phi_H)}^{F_1(\phi_2)} e^{-jkr}[-\Psi_7(r)]\,dr + \int_{F_2(\phi_H)}^{F_2(\phi_2)} e^{-jkr}[\Psi_8(r)]\,dr + \int_{F_1(\phi_2)}^{F_2(\phi_2)} e^{-jkr} \times[-\Psi_9(r)]\,dr + \int_{F_1(\phi_H)}^{F_2(\phi_H)} e^{-jkr}[\Psi_{10}(r)]\,dr\right]. \tag{A17}$$

[1]M. Arditi, F. Foster, and J. Hunt, "Transient fields of concave annular arrays," Ultrason. Imaging **3**, 37–61 (1981).

[2]P. R. Stepanishen, "The time-dependent force and radiation impedance on a piston in a rigid infinite planar baffle," J. Acoust. Soc. Am. **49**, 841–849 (1971).

[3]P. R. Stepanishen, "Transient radiation from pistons in an infinite planar baffle," J. Acoust. Soc. Am. **49**, 1627–1638 (1971).

[4]P. Wu and T. Stepinski, "Spatial impulse response method for predicting pulse-echo fields from a linear array with cylindrically concave surface," IEEE Trans. Ultrason. Ferroelectr. Freq. Control **46**, 1283–1299 (1999).

[5]J. A. Jensen, "Field: A Program for Simulating Ultrasound Systems," *10th Nordic-Baltic Conference on Biomedical Imaging, Medical & Biological Engineering & Computing*, Vol. **34**, Suppl. 1, Part 1, pp. 351–353 (1996).

[6]T. L. Szabo, *Diagnostic Ultrasound Imaging Inside Out* (Elsevier Academic, Amsterdam, 2004), p. 157.

[7]B. Piwakowski and K. Sbai, "A new approach to calculate the field radiated from arbitrarily structured transducer arrays," IEEE Trans. Ultrason. Ferroelectr. Freq. Control **46**, 422–440 (1999).

[8]P. R. Stepanishen and K. C. Benjamin, "Forward and backward projection of acoustic fields using FFT methods," J. Acoust. Soc. Am. **71**, 803–812 (1982).

[9]J. F. Theumann, M. Arditi, J. J. Meister, and E. Jaques, "Acoustic fields of concave cylindrical transducers," J. Acoust. Soc. Am. **88**, 1160–1169 (1990).

[10]G. Tupholme, "Generation of acoustic pulses by baffled plane pistons," Mathematika **16**, 209–224 (1969).

[11]T. L. Szabo, "Time domain wave equations for lossy media obeying a frequency power law," J. Acoust. Soc. Am. **96**, 491–500 (1994).

[12]B. U. Karbeyaz, "Modeling and shape based inversion for frequency domain ultrasonic monitoring of cancer treatment," Ph.D. thesis, Northeastern University, Boston, MA.

[13]I. Gradshteyn and I. Ryzhik, *Table of Integrals, Series, and Products* (Academic, New York, 2000).

[14]N. S. Bakhvalov and L. G. Vasil'eva, "Evaluation of the integrals of oscillating functions by interpolation at nodes of gaussian quadratures," USSR Comput. Math. Math. Phys. **8**, 241–249 (1968).

[15]C. A. Balanis, *Advanced Engineering Electromagnetics* (Wiley, New York, 1989).